Technical Physics, 2025, Vol. 70, No. 4

04

Numerical and experimental study of laser initiated microwave discharge trace temperature

© M.E. Renev, Yu.V. Dobrov, V.A. Lashkov, N.D. Osipov, I.Ch. Mashek, R.S. Khoronzhuk

St. Petersburg State University,
199034 St. Petersburg, Russia
e-mail: renevme@mail.ru

Received December 10, 2024
Revised December 10, 2024
Accepted December 10, 2024

A numerical and experimental study of the trace temperature of a microwave discharge initiated by a laser in air is carried out. The amplitude of the microwave field strength is 2.0 kV/cm, discharge is ignited at pressures up to 6.66 kPa; the duration of the microwave radiation pulse is 2.5 μs. The use of 10 ns laser pulses with an energy of 200 mJ and a wavelength of 532 nm makes it possible to obtain an initiated subcritical microwave discharge at a pressure of 10.6 kPa. The dependences of the discharge trace temperature on time with initiation up to 200 μs and a pressure of 5.33–10.0 kPa are given. The trace of the discharge is hot, the temperature is about 1000 K, which corresponds to the trace of a filament discharge. The numerical model confirms the possibility of obtaining a filament subcritical microwave discharge at low pressures of about 10 kPa in a few μs due to laser initiation. The model is based on those known in the literature and is modified with explicit consideration of photoeffects during the solution. The consistency of the results of trace temperature calculations and interferometry, taking into account the uncertainty of 25 %, is achieved in the first 20 μs after switching off the microwave radiation.

Keywords: Heating, plasma, hydrodynamic model, Fabry-Perot interferometer, laser initiation, microwave radiation.

DOI: 10.61011/TP.2025.04.61206.450-24

Introduction

Plasma, that may heat the medium, initiate chemical reactions and generate radiation, has many applications. Plasma may be used for plasma conversion of fuel [1], plasma ignition and burning of mixtures [2,3], as well to control gas-dynamic flotations and body floatation [4,5]. The higher the temperature and degree of ionization, the stronger the plasma effect.

One of the methods for producing gas-discharge plasma is the use of strong very-high frequency (microwave-MW) radiation. The Paschen curve allows determining the required power to produce a discharge under specified conditions: pressure, composition of the medium [6]. A seed electron is needed, from which an electron avalanche will develop in a powerful electric field. Over time, the number of electrons will increase, and the external electric field will be distorted by the avalanche. An avalanche-streamer transition will occur with the appearance of the streamer. At low pressure this transition is initially diffusive. This type of discharge is characterized by relatively large transverse dimensions, as well as gradually changing characteristics: luminescence, Joule heating, medium temperature, etc.

An important further stage in the development of the discharge for rapid energy input into supersonic flows and ignition of fuel mixtures is the filament stage. Filaments [7,8] are the narrow hot (constricted) plasma channels. Their formation is associated with ionization-overheating instability [6,9]. Over time, the temperature in plasma increases, the conductivity goes up, the Joule heating power grows, and then the temperature rises even faster, etc. The process of instability development accelerates. The initially diffusive „wide“ streamer becomes filamentous. Filaments are distinguished by high temperature: not less than 1000 K [8,10].

The duration of transition to the filament phase significantly depends on power and frequency of the radiation, and on pressure of the medium. With a decrease in radiation pressure and power, it is more difficult to obtain filament phases. The typical waiting time of the filament phase is approximately 10 μs at a pressure of 6.66 kPa and radiation frequency of 7.5 GHz, MW intensity of 3.4 kV/cm [8.10].

In the framework of this study, it is important to consider examination in theoretical and numerical analysis of the properties of a microwave discharge. A number of them use experimental data directly and allow them to be processed. In papers [11,12] , the relations between the experimental plasma dimensions and its averaged properties are derived. A semi-analytical one-dimensional model is presented in paper [13] for describing a microwave plasmoid, reproducing the known dynamics of a microwave discharge and experimental data. However, it is difficult to add certain effects to the models of this type. There are numerical models with a large number of equations and complex analysis that may analyze the discharge dynamics and plasma effects individually using basic equations and general material properties [8,14–16]. Such models allow accounting for various sets of reactions depending on the study purpose.

Studies are known describing „Fast gas heating“ by plasma [4,17–20]. In the non-equilibrium plasma with powerful nanosecond power (including microwave [21]), the hot electron gas creates intensely excited states of components that can transfer energy to the medium during further reactions. The effect of accelerating such reactions in the presence of atomic oxygen is noted [22].

Focused laser radiation ensures reactions of the multiphoton or tunneling ionization occurring in the media [23]. In the first case, the frequency of the photoionization reaction significantly depends on the wavelength of the laser radiation. In a short time, several photons with a total energy sufficient to ionize the target molecule should enter it. The longer the wavelength, the more photons are needed, and the more difficult it is for all of them to hit the target in a short period of time. Higher intensity of laser radiation simplifies this process, and the frequency of photoionization increases exponentially [24]. With a certain intensity, the strength of the laser radiation becomes high enough so that the probability of an electron detachment from the molecule and its overcoming the potential barrier of Coulomb's force as a quantum object becomes noticeable. This process does not depend on the wavelength of the radiation and the energy of a single photon. Keldysh number γ — ratio of the frequency of laser light ω_{las} to the frequency of electron tunneling through a potential barrier

$$\gamma = \frac{\omega_{las}\sqrt{2m_e I}}{eE_{las}},$$

where m_e and e — the mass of the electron and elementary charge, I — the ionization potential of the atomic level, E_{las} — the amplitude of the electric field of laser radiation. This number is used to determine the choice between the two studied photoionization mechanisms. For the multiphoton ionization, it shall be greater than one.

Intensive photo-ionization will definitely change the development of a microwave discharge. The stages of avalanche development and transition to the filament form may be skipped or significantly shortened. MW discharge may start to develop from a highly ionized trace of a laser spark already significantly heated [25,26]. It is also known [25], that on an extended conductive laser track (without a spark) it is possible to obtain a microwave discharge with a reduced ignition threshold in terms of radiation power. In the study [27], filamentous microwave discharges were obtained in a waveguide with a fuel mixture; with the help of femtosecond laser radiation, the ignition threshold was lowered by 50 %, ignition of the methane-air fuel mixture was ensured, which should mean a sufficient level of energy input into the mixture, despite the reduced radiation power.

Numerical models of laser radiation are available in the literature [28], in which the distribution of laser radiation intensity is calculated using optics equations. A more cost-effective alternative may be to specify the analytical distribution [29], suitable in case of negligible absorption of radiation by the medium. The intensity distribution is necessary to calculate the rates of photo-reactions. The tunnel ionization model [30–33] is used if Keldysh parameter is less than one. The authors of this paper have previously searched for a way to simplify the dependence of the multiphoton ionization rate [29], based on the analysis of the dependence of this rate on the wavelength outlined in [24]. Keldysh number was above 3 in this study. In general, it is customary to use quantum equations as the basis for analysis [23].

In this paper, the temperature of the MW discharge trace with a sparkless laser initiation is investigated numerically and experimentally. The amplitude in focus and the frequency of the microwave field electric strength are 2.0 kV/cm and 9.6 GHz. The focal area for the microwave is defined as a spheroid with major and minor semi-axes of 30 and 5 mm. The MW pulse duration (trapezoid with fronts of 200 ns) is equal at half maximum to 2.5 μs. Laser beam goes parallel to the vector of MW-radiation electrical strength. The laser pulses have an energy of 200 mJ, with duration of 10 ns, wavelength of 532 nm and are focused by a lens with a focal length of 250 mm. The microwave and laser foci are combined. Laser radiation time is 300 ns. Initially, without laser radiation, MW discharge can be generated at a pressure of no more than 6.66 kPa under specified conditions. Laser initiation allows rising the threshold pressure of up to 10.6 kPa. MW discharge with laser initiation at pressure of 5.33−10.0 kPa is studied. Numerical modeling is based on the extensive hydrodynamic plasma model [29]. Non-stationary equations of components transfer with reactions, electron gas equations, Helmholtz and Navier-Stokes equations for a compressible medium are solved jointly. In this experiment, the temperature of the discharge trace is measured using a Fabry-Perot interferometer.

1. Numeric modelling setting

1.1. System of equations

The task is to calculate the temperature of the microwave discharge trace with a sparkless laser initiation, where definitions of laser effects from [9] have been added to the well-known model [10] in the form of additional reactions for the electron gas. The following gas medium components are considered: N_2, O_2, N_2^+, O_2^+, O, O^+, O_2^-, O^-, $O_2(\alpha_1\Delta)$, $N_2(A)$, $N_2(a)$, N, N^+. The system of equations was written as follows:

$$\frac{\partial n_e}{\partial t} + \nabla \cdot \mathbf{J}_e = S_e, \quad \mathbf{J}_e = -D_e \nabla n_e + (\mathbf{V}_g, \nabla) n_e,$$

$$\frac{\partial n_e \psi}{\partial t} + \nabla \cdot \mathbf{J}_\psi = S_\psi + Q_{ext},$$

$$\mathbf{J}_\psi = -D_\psi \nabla \psi n_e + (\mathbf{V}_g, \nabla) \psi n_e,$$

$$\rho_g \frac{\partial w_i}{\partial t} + \nabla \cdot \mathbf{J}_i + \rho_g (\mathbf{V}_g, \nabla) w_i = S_i,$$

$$\mathbf{J}_i = -\rho_g w_i D_i \ln(w_i M_g), \quad w_{N_2} = 1 - \sum_{i \neq N_2} w_i,$$

$$\rho_g = \frac{\rho_g M_g}{RT_g}, \quad \frac{\partial \rho_g}{\partial t} + \nabla(\rho_g \mathbf{V}_g) = 0,$$

$$\rho_g \frac{\partial \mathbf{V}_g}{\partial t} + \rho_g(\mathbf{V}_g, \nabla)\mathbf{V}_g = -\nabla \rho_g - \nabla \mathbf{K}_g,$$

$$\mathbf{K}_g = \mu_g \left(\nabla \mathbf{V}_g + (\nabla \mathbf{V}_g)^T - \frac{2}{3}(\nabla, \mathbf{V}_g) I \right),$$

$$\rho_g C_p \left(\frac{\partial T_g}{\partial t} + \mathbf{V}_g \nabla T_g \right) - k_g \nabla T_g = Q_g,$$

$$\nabla \times [\nabla \times \mathbf{E}_{MW}] - k_{MW}^2 \left(\left(1 - \frac{i\sigma_{plas}}{\omega_{MW}\varepsilon_0} \right) \mathbf{E}_{MW} - \frac{i\mathbf{J}_{MW}^{ext}}{\omega_{MW}\varepsilon_0} \right) = 0,$$

$$\sigma_{plas} = |e| \left(b_e n_e + \sum_i z_i^2 b_i n_i \right), \quad n_i = \frac{N_A}{M_i} \rho_g w_i,$$

where t — time; n_e — concentration of electrons; ψ — average thermal energy of electrons; $\mathbf{J}_e$ and $\mathbf{J}_\psi$ — vectors of electron fluxes, electron energy; S_e and S_ψ — sources of electrons and electron energies generated due to plasma reactions; Q_{ext} — external source of electrons energy; b_e — electrons mobility coefficient (complex coefficient, allowing for variable electrical field); D_e and D_ψ — electrons diffusion constants, electron energy constants; w_i — mass fraction of neutral component or ion component (sort i); $\mathbf{J}_i$ — vector of component flux i; S_i — source of component i; z_i — relative charge of component i; b_i — component mobility i; n_i — component concentration i; D_i — component diffusion constant i; ρ_g — mass density of gas medium; $\mathbf{V}_g$ — velocity of the medium; M_g — molar mass of the medium; M_i — molar mass of individual component; p_g — static pressure of the medium; T_g — static temperature of the medium; C_p — isobar specific heat capacity of the medium; k_g — thermal conductivity coefficient of the medium; $\mathbf{K}_g$ — tensor of viscous stresses of the medium; μ_g — tensor of dynamic viscosity stresses of the medium; Q_g — gas energy source; $\mathbf{E}_{MW}$ — MW field vector; k_{MW} — MW field wavenumber; ω_{MW} — radiation frequency; σ_{plas} — plasma conductivity; ε_0 — electrical constant; $\mathbf{J}_{MW}^{ext}$ — density of external electrical field (to generate MW field from antenna); R — universal gas constant; N_A — Avogadro number; $|e|$ — elementary charge; $\mathbf{I}$ — unit matrix 3×3; i — imaginary unit.

An axisymmetric two-dimensional model is used, coordinates r and z, center of the coordinate system — focus of laser and MW radiation. The geometry is provided in Fig. 1, *a*. MW-radiation (Fig. 1, *b*) is generated using a volumetric source J_{MW}^{ext}:

$$\mathbf{J}_{MW}^{ext} = \omega_{MW}\varepsilon_0 \mathbf{E}_{MW}^{ext}(r, z, t) = \omega_{MW}\varepsilon_0 E_0 \mathbf{e}_z f_{Et}(t) f_{Erz}(r, z),$$

$$f_E(t) = \begin{cases} 0, & t < t_0 \\ \frac{t-t_0}{t_1-t_0}, & t_0 \le t < t_1 \\ 1, & t_1 \le t < t_2 \\ \frac{t_3-t}{t_3-t_2}, & t_2 \le t < t_3 \\ 0, & t_3 < t, \end{cases}$$

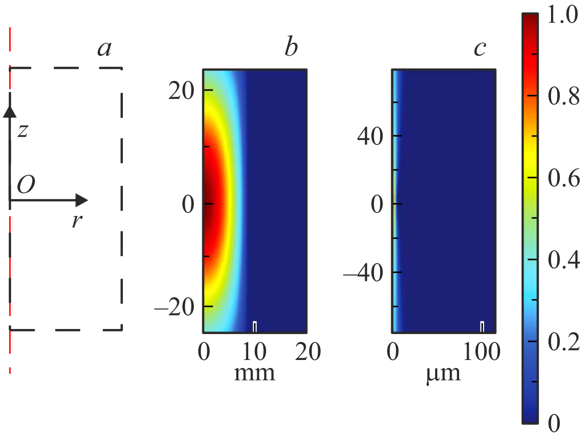

Figure 1. *a* — model geometry (20 × 50 mm), *b* — distribution of MW field strength with an amplitude of 1 V/m, *c* — normalized distribution of laser emission intensity at a pulse of 100 mJ (maximum $2 \cdot 10^{13}$ W/cm^2).

$$f_{Erz}(r, z) = \left(\sin c \left(\frac{a k_{MW} z}{2} \right) \right)^2 \left(1 - \left(R^{-1} \min(r, R) \right)^2 \right),$$

where E_0 — amplitude of electrical component of the MW-field $\mathbf{e}_z$ — unit axis z (linear polarization, electric field is oriented along the axis z), $f_E(t)$ — and $f_{Erz}(r, z)$ — time and spatial dependencies of the electric field. Parameters t_0, t_1, t_2, t_3 are equal, accordingly 0, 0.2, 2.5 and 2.7 μs (square pulse 2.5 μs with leading and trailing edges of 200 ns). The amplitude E_0 and parameters a, R were selected to match the experimental conditions and experimental antenna (the elliptical antenna and the horn were analyzed separately to obtain data for approximating the microwave field in the main focus).

Laser radiation (Fig. 1, *c*) is defined as a fixed intensity distribution I_{las} corresponding to the pulse energy $Q_{las} = 100$ mJ, duration (Gaussian distribution with half maximum width τ_{las}) 10 ns, focal length of the collecting lens of $F = 250$ mm, distance from the laser to the lens of $d = 1$ m. The laser pulse is applied after 100 ns ($t_{las} = 300$ ns) after the end of the microwave leading edge. Formulae to approximate the intensity of laser radiation

$$I_{las}(r, z, t) = Q_{las} C_{norm} f_1(t) f_2(r, z),$$

$$\int_{-\infty}^{\infty} dt \int_0^{\infty} C_{norm} f_1(t) f_1(r, 0) 2\pi r dr = 1,$$

$$f_1(t) = \exp\left(-\frac{(t - t_{las})^2}{(\tau_{las}/2)^2} \right),$$

$$f_2(r, z) = \sqrt{\frac{k_{las}}{q_{las} + z}} \exp\left(-\frac{1}{2} \frac{k_{las} r^2}{q_{las} + z} \right),$$

$$k_{las} = \frac{2\pi}{\lambda_{las}},$$

$$q_{las} = \sqrt{D_F \frac{r_f^2}{r_f^2 + k_{las}^2 D_F}},$$

$$D_F = r_0^2 + \frac{d^2}{k_{las}^2 r_0^2},$$

$$\frac{1}{r_F} = \frac{1}{F} - \frac{1}{R_F},$$

$$R_F = d + \frac{(k_{las}^2 r_0^2)^2}{d},$$

where C_{norm} — normalization constant (full energy passed through the cross-section $z = \text{const}$, shall be equal to the energy of pulse), $f_1(t)$ and $f_2(r, z)$ — temporal (1/s) and spatial (1/m^2) components of the laser radiation intensity distribution, k_{las} — wavenumber of laser radiation (wavelength of λ_{las} 532 nm), r_0 — laser hole radius, q_{las} — parameter of the radius of laser beam in focus, R_F and r_F — curvature radii of the radiation phase surface upstream and downstream the lens, D_F — parameter standing for the laser beam area at lens prior to focusing.

The effective laser field can be calculated from the intensity of laser radiation, polarization of the laser radiation is linear [4]:

$$E_{las}^{\text{eff}} = \frac{\nu_e}{\left(\nu_e^2 + f_{las}^2\right)^{\frac{1}{2}}} \sqrt{377[\Omega] I_{las}(r, z, t)},$$

where ν_e — frequency of electrons collision with neutral particles, f_{las} — frequency of laser radiation, 377 Ω — wave resistance of vacuum.

Reactions pattern is given in the Table. For the photoionization they used approximations of the ionization frequency as functions ax^b, where x — normalized at 1 W/cm^2 intensity of radiation I_{las}. The photo-stripping frequencies are described by the functions $aI_{las}/h\nu$. The frequencies of photoionization and photo-stripping are multiplied by the concentrations of neutral components to calculate the reaction rates. The reactions cross-section is set for a number of reactions with an electron, from which the coefficient is calculated. For such reactions, instead of the coefficient, „approximation“ is written.

The material properties of individual components of the medium are embedded in Comsol numerical modeling package used. According to the mixing rule, the heat capacity, thermal conductivity coefficients, and viscosity of the entire medium are calculated. The value Q_g is determined from the sum of the Joule heating capacities by ions of the medium and exothermic-endothermic reactions in the medium under the action of plasma. Enthalpies of the formed substance from [44] were taken to calculate the reactions heat.

1.2. Initial and boundary conditions

At the initial moment of time the gas medium in terms of its composition is more like air, with uniform pressure p_{g0} varying by parameters from 5.33 to 10.0 kPa, temperature T_{g0} equals to 293 K, concentration of electrons n_{e0} equals to 10^{12} 1/m^3, average energy of an electronψ_0 makes 0.04 eV.

Vector $\mathbf{e}_r$ — unit vector for axis r. Axis z — axis of symmetry, boundary conditions are set here:

$$(\mathbf{J}_k, \mathbf{e}_r) = 0, k \in \{e, \psi, i\};$$

$$(\mathbf{V}_g, \mathbf{e}_r) = 0, \quad \nabla_r p_g = 0, \nabla_r T_g, ||\mathbf{E}_{MW}|| < \infty.$$

On other boundaries, marked as dashed lines in Fig. 1, *a*, the following conditions are set

$$n_e = n_{e0}, \ \psi = \psi_0, \ w_{N_2} = 0.8, \ w_{O_2} = 0.2,$$

$$w_{i \neq N_2, O_2} = 0, \ p_g = p_{g0}, \ T_g = T_{g0},$$

$$\mathbf{n} \times [\nabla \times \mathbf{E}_{MW}] = \left(ik_{MW} + \frac{1}{2r}\right) \mathbf{n} \times [\mathbf{E}_{MW} \times \mathbf{n}]$$

$$+ \frac{\nabla\left[[\nabla \times \mathbf{E}_{MW}]_{\mathbf{n}} \mathbf{n}\right]}{2ik_{MW} + 1/r},$$

where $\mathbf{n}$ — vector perpendicular to the boundary.

1.3. Numerical method

Comsol Multiphysics software was used for analysis. Numerical method — finite element method. A rectangular grid is built for spatial discretization of the equations. The grid elements are linear, their number is 240 thousands. In direction from the outer boundaries to the center of coordinates (radiation foci), the elements decrease exponentially. The ratio of the largest and the lowest lengths of the elements facet along the axis r is 2000, along the axis z — 200. The lowest element is $0.25 \times 1.5\,\mu$m in size. The system of equations is solved iteratively by replacing nonlinear equations with linearized ones: all nonlinear terms are transformed into linear ones with a constant multiplier that is defined during iterations.

For time integration, a method with backward differentiation formulae with an order of 2 or 3 is used. Courant number for the entire grid did not exceed 10. The value of the derivatives in the equations was monitored so that during the time step the desired values did not change by more than 0.1 % relative to the previously selected scale parameters. They are introduced for each considered variable. Scales: MW field amplitude of 2 kV/cm, electron concentration 10^{20} 1/m^3, average electron gas energy of 1 eV, mass fractions of medium components equal to one, pressure of 5.33 kPa, medium velocity of 100 m/s, medium temperature of 293 K. In the event that convergence of the solution was not achieved at the time step, or the Courant number or threshold for changes in the desired values was exceeded, the program automatically reduced the step and the order of the method to the second, otherwise it increased the step and the order of the method to the third. At the moment when the laser pulse was applied, as well as after plasma ignition and before the microwave

Table 1. Plasma-chemical reactions pattern

№	Pattern	Type	Coefficient, 1/s, 1/cm^3/s, 1/cm^6/s	Reference
1	$h\nu+O_2=O_2^+ + e$	Photo-ionization	$a = 1.36 \cdot 10^{-48}[s^{-1}]$, $b = 4.41$	[24,29]
2	$h\nu+N_2=N_2^+ + e$	Photo-ionization	$a = 1.733 \cdot 10^{-77}[s^{-1}]$, $b = 6.373$	[24,29]
3	$h\nu+O_2^-=O_2 + e$	Photo-stripping	$a = 1.3 \cdot 10^{-18}[cm^2]$	[29,34]
4	$h\nu+O^-=O+e$	Photo-stripping	$a = 7.3 \cdot 10^{-18}[cm^2]$	[29,34]
5	$e + A = e + A^*$, $A \in \{O_2,N_2,O,N\}$	Excitation[1]	Approximation	[35,36]
6	$e+O_2 = e+O_2(\alpha_1\Delta)$	Excitation	Approximation	[36]
7	$e+N_2 = e+N_2(a)$	Excitation	Approximation	[36]
8	$e+N_2 = e+N_2(A)$	Excitation	Approximation	[36]
9	$O_2(\alpha_1\Delta) =O_2$	Relaxation	1/2700	[6]
10	$N_2(a) =N_2$	Relaxation	1/0.5	[6]
11	$N_2(A) =N_2$	Relaxation	1/2	[6]
12	$e+O_2 = 2e+O_2^+$	Ionization	Approximation	[37]
13	$e+O_2(\alpha_1\Delta) = 2e+O_2^+$	Ionization	Approximation	[38]
14	$e+N_2 = 2e+N_2^+$	Ionization	Approximation	[36]
15	$e+N_2(A) = 2e+N_2^+$	Ionization	Approximation	[39]
16	$e+N_2(a) = 2e+N_2^+$	Ionization	Approximation	[39]
17	$e+O_2 = 2e+O+O^+$	Ionization	Approximation	[37]
18	$e+N_2 = 2e+N+N^+$	Ionization	Approximation	[37]
19	$e+O=2e+O^+$	Ionization	Approximation	[36]
20	$e+N=2e+N^+$	Ionization	Approximation	[40]
21	$e+O_2=O+O^-$	Sticking	Approximation	[37]
22	$e+O_2+M=O_2^-+M$	Sticking	Approximation	[35]
23	$e+O_2(\alpha_1\Delta)=O^-+O$	Sticking	Approximation	[39]
24	$e+O^-=2e+O$	Stripping	Approximation	[39]
25	$O^-+O=e+O_2$	Stripping	$2 \cdot 10^{-10}(T_g/300[K])^{0.5}$	[41]
26	$e+O_2^++M=O_2+M$	Electron-ion recombination	$2.49 \cdot 10^{-41}(1[eV]/T_e)^{1.5}$	[42]
27	$e+N_2^++M=N_2+M$	Electron-ion recombination	$6 \cdot 10^{-27}(300[K]/T_e)^{1.5}$	[42]
28	$e+O^++M=O+M$	Electron-ion recombination	$6 \cdot 10^{-27}(300[K]/T_e)^{1.5}$	[42][2]
29	$e+N^++M=N+M$	Electron-ion recombination	$6 \cdot 10^{-27}(300[K]/T_e)^{1.5}$	[42][2]
30	$O_2^-+O_2^+ =O_2+O_2$	Ion-ion recombination	$4.2 \cdot 10^{-27}(300[K]/T_e)^{0.5}$	[6]
31	$O_2^-+O^+ =O_2+O$	Ion-ion recombination	$2 \cdot 10^{-27}(300[K]/T_e)^{0.5}$	[6]
32	$O_2^-+N_2^+ =O_2+N_2$	Ion-ion recombination	$1.6 \cdot 10^{-27}(300[K]/T_e)^{0.5}$	[6]
33	$O_2^-+N^+ =O_2+N$	Ion-ion recombination	$4.2 \cdot 10^{-27}(300[K]/T_e)^{0.5}$	[6]
34	$O^-+O^+ =O+O_2$	Ion-ion recombination	$1 \cdot 10^{-7}(300[K]/T_e)^{0.5}$	[6]
35	$O^-+O^+=O+O$	Ion-ion recombination	$2.7 \cdot 10^{-7}(300[K]/T_e)^{0.5}$	[6]
36	$O^-+N_2^+=O+N_2$	Ion-ion recombination	$4.2 \cdot 10^{-7}(300[K]/T_e)^{0.5}$	[6]
37	$O^-+N^+=O+N$	Ion-ion recombination	$4.2 \cdot 10^{-7}(300[K]/T_e)^{0.5}$	[6]
38	$O+O=O_2^+ + e$	Ionization	$1.8 \cdot 10^{-21}(T_g/1[K])^{2.7} \cdot \exp(-80600[K]/T_g)$	[43]
39	$N+N=N_2^+ + e$	Ionization	$1.8 \cdot 10^{-21}(T_g/1[K])^{2.7} \cdot \exp(-80600[K]/T_g)$	[43]
40	$O+O+M=O_2^++M$	Association	$2.45 \cdot 10^{-31}(T_g/1[K])^{-0.63}$	[43]

[1] 66 reactions are set to clarify the energy of electrons without formation of products (reactions with meta-stable states are recorded separately).

[2] Generalized from data from reactions [26,27].

field was turned off, the time step was on average 0.01 ns. The method of separation of variables (groups of variables) is used to solve the system of algebraic equations: MW field, electron gas, all ions, neutral components, velocity and pressure of the medium, temperature of the medium) and the PARDISO method (modification of the Gauss method) [45].

2. Setting up the experiment

The test was carried out in the Eiffel chamber. Fig. 2 shows the laboratory setup (Fig. 2, *a*) and its photo (Fig. 2, *b*). Microwave radiation is generated by the magnetron MI-505, fed to the horn in the chamber. The horn emits a conically diverging wave, which is then reflected from an elliptical-shaped metal surface (antenna), and a standing electromagnetic wave with multiple antinodes with different amplitudes is generated. The major antinode „focus" is located 90 mm away from the edge of the waveguide. Laser radiation: A pulse from Quantel Evergreen 200 laser is fed through a prism and lens into the camera to the studied area. The last prism is installed under the lens in „model ": a metal streamlined shell with the possibility of further installing plastic nozzles on it for the tasks of supersonic gas dynamics with energy input. The combination of focus with smoke and photography was checked.

Preliminary experiments with obtaining a microwave discharge without laser initiation at different pressures have shown that the discharge ignites at pressure no greater than 6.66 kPa. Based on this, the amplitude of the MW field strength in focus of 2.0 kV/cm was selected for numerical modelling. Using laser initiation, the discharge was ignited at a pressure of up to 10.6 kPa.

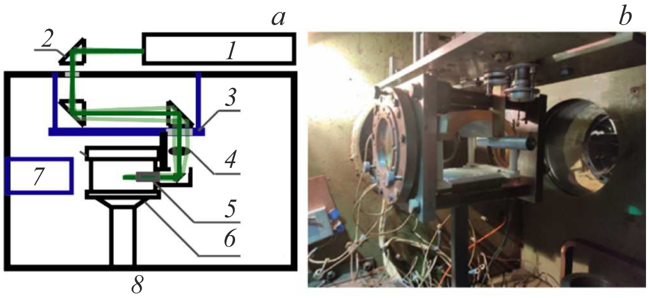

Figure 2. The system of receiving laser and microwave radiation in the Eiffel chamber: optical circuit (*a*), laboratory setup (*b*). *1* — laser, *2* — prism, *3* — rack, *4* — lens, *5* — model, *6* — MW antenna, *7* — nozzle, *8* — vacuum chamber.

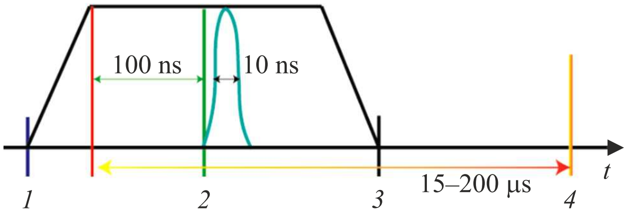

Figure 3. Sequence of control signals (not to scale): *1* — MW activation, *2* — activation of laser pulse, *3* — MW is deactivated, *4* — signal to photo-camera. Time of MW rise and decline is 0.2 μs, duration of MW pulse 2.5 μs.

To measure the temperature of the trace, a multipath Fabry-Perot interferometer was used (shown in Fig. 2, *b*) in conjunction with the optical circuit of IAB 451 heater. According to the methodology [46] it is known how to calculate the distortion of interferometer bands based on a given axisymmetric temperature inhomogeneity. When deciphering the interferometry, the authors numerically solved the inverse problem.

The experimental equipment was controlled using LabVIEW program and National instruments equipment. The control signals were supplied (Fig. 3) to the MW generator, laser and video camera PCO DiCAM-PRO GaAs P46 with a resolution of 1024 × 1024, exposure time of 5 μs. The video camera recorded one photo of interferometry (example in Fig. 4) within a single system launch. For the selected pressure, a number of system launches were performed with different shooting times. This resulted in interferograms for different MW discharges in the time range from 15 to 200 μs in increments of 5 μs. The assumption is made that MW discharges are identical between repetitions under the same conditions, which makes it possible to measure the temperature dependence of the discharge trace on time.

The discharge trace could provide a distortion of up to two interferometer fringes (Fig. 4). The distance between the considered fringes was 8 mm. During the experiment, the pressure in Eiffel chamber was manually adjusted to an accuracy of 0.33 kPa. The interference pattern was digitized for further mathematical processing. During processing, data was also entered with the addition of pressure uncertainty, which made it possible to estimate the temperature uncertainty: no more than 25%.

3. Analysis of results

Let's consider the laser-induced MW discharge at pressure of 5.33 kPa. This is a supercritical discharge, since pressure is below the ignition threshold of 6.66 kPa for a microwave discharge without initiation. The numerical model showed that a laser pulse creates a conducting channel with a maximum electron concentration of about $4.7 \cdot 10^{20}$ 1/m^3 and a length of 360 μm in terms of specific conductivity of 10 S/m. The magnitude of the conductivity and the size of the conducting zone are considered, since this directly affects the redistribution of external microwave radiation to the edges of plasma and its growth in length. The concentration of electrons first drops to $2 \cdot 10^{19}$ 1/m^3 because of deactivation of the laser radiation. Then, it rises to $2.6 \cdot 10^{20}$ 1/m^3 due to heating of the medium by plasma. In this case, the region of high electron concentration becomes long and thin: at half maximum the length is 4.0 mm and the radius is 0.4 mm. At 5.33 kPa the Joule heating energy of 18.2 mJ made its contribution to both, the

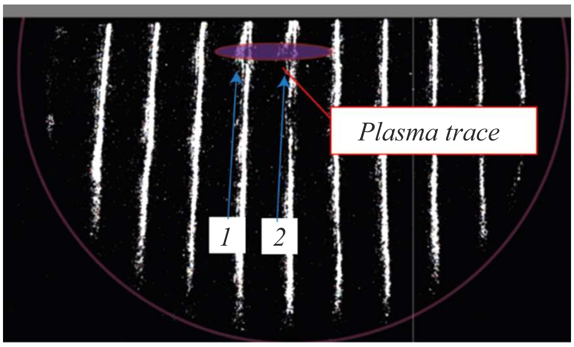

Figure 4. Interference pattern (15 μs after the start of the experiment) for the trace of the initiated MW discharge (5.33 kPa, 200 mJ, laser pulse delay of 100 ns). Plasma distorts two fringes with numbers *1, 2*.

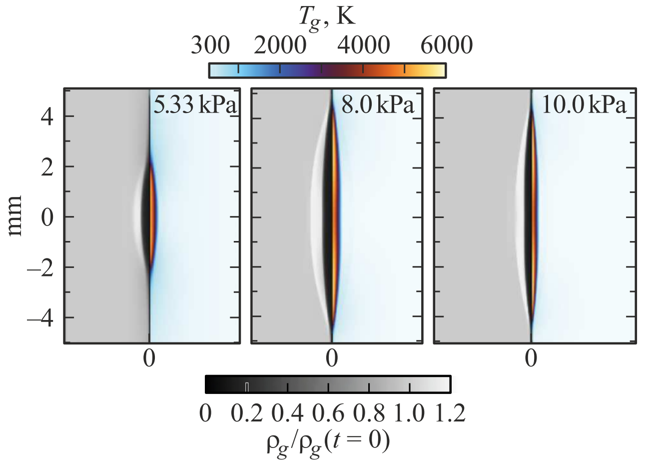

Figure 5. Distribution of the normalized density and temperature of the medium after exposure to the initiated MW-discharge by the end of MW-pulse for pressures 5.33, 8.0 and 10.0 kPa.

electron gas and the ionized air. Of these, by the end of the microwave pulse, 1.4 mJ is put in the air — chemical and Joule heating by ion current. As a result, by the time MW-radiation is turned off, the air temperature is 5000 K, and its density is reduced to 6% relative to the initial one (Fig. 5). The resulting initiation discharge is filamentous in terms of high temperature and electron concentration.

Subcritical initiated and threshold (6.66 kPa) MW-discharges differ significantly from supercritical discharges in length (Fig. 5). It is practically the same for them and is equal 7.4 – 8.4 mm, which is twofold higher than at 5.33 kPa. This is due to the fact that the laser pulse with the same energy produced a channel with a higher maximal concentration of electrons $1-2\cdot10^{21}$ 1/m^3 (by 2–4 times higher), the length of the channel increased from 0.36 to 0.46 – 0.65 mm. The channel variation is caused by a rise in the absorption coefficient of laser radiation with increasing pressure. Characteristic temperatures of the medium after MW-discharge are equal 5500–6000 K. With increasing pressure, the energy input shrinks to 6.7 mJ (10.0 kPa), of which 0.4 mJ is invested directly into the medium through ion currents and chemical reactions by the end of the pulse. Sub-critical discharges are also filamentous. Laser radiation, obviously, significantly accelerates discharge filamentation even at such low pressures as 5.33–10.0 kPa, and an electric field of microwave radiation of 2.0 kV/cm.

Overheating temperature (trace) –the difference between the temperatures of the medium at the considered and initial moment of time (293 K) before the appearance of plasma. Fig. 6 and 7 illustrate the overheating temperatures from the numerical modelling along *r, z* axes for pressure level of 5.33–10.0 kPa and time moments from 3 to 25 μs relative to the start of MW-radiation supply (Fig. 3). The trace of super-critical MW-discharge with initiation (blue line) in the first 2–3 μs after MW radiation deactivation rapidly cools down 2200 K — 2 times less than the initial 5000 K. The rate of temperature variation further slows down. By 25 μs the trace overheating temperature is equal 650 K. By 25 μs the trace diameter on half of the overheating temperature increases from 0.5 to 1.0 mm, the trace length — from 4.0 to 5.2 mm.

In traces of subcritical MW-discharges (Fig. 6 and 7, red and black lines), the overheating temperature also decreases twofold in 2 – 3 μs, and then the rate of temperature variation goes down. At higher pressure the trace cools down faster. The radius of such traces increased over time in the same way as that of the trace at 5.33 kPa. The length of the traces along the half of the overheating temperature

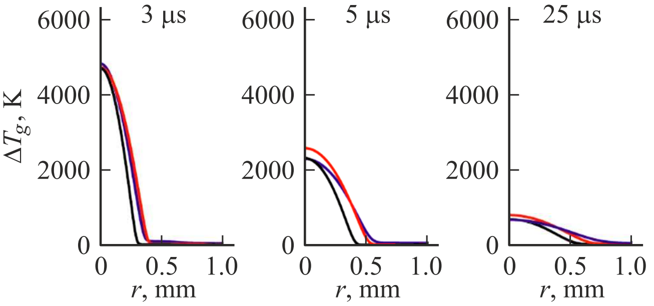

Figure 6. Distribution of the overheating temperature along *r* axis for pressure level of 5.33 (blue line), 8.0 (red line) and 10.0 kPa (black line) at various moments of time. 3 – 25 μs.

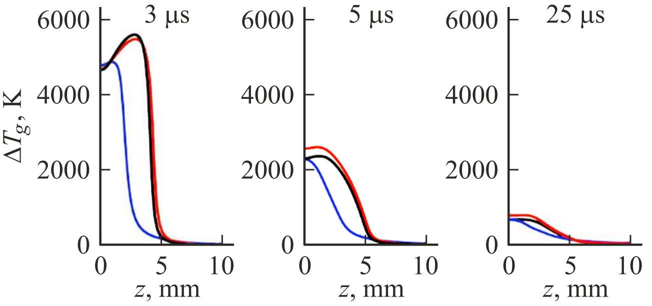

Figure 7. Distribution of the overheating temperature along *z* axis for pressure level of 5.33 (blue line), 8.0 (red line) and 10.0 kPa (black line) at various moments of time3 – 25 μs.

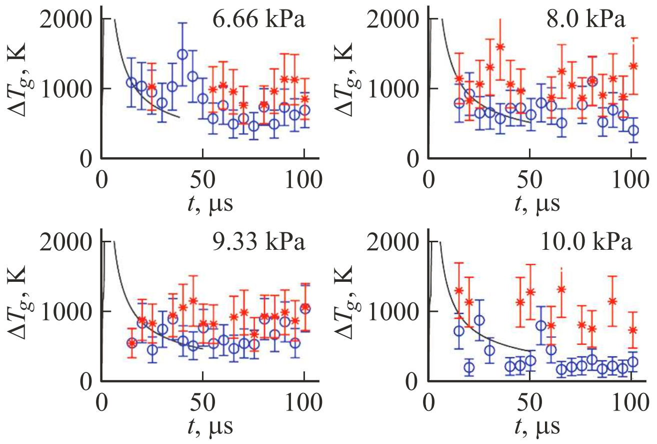

Figure 8. The maximum overheating temperature from the model (black lines) and the overheating temperatures measured by the interferometer on the fringes *1* (red dots) and *2* (blue dots) at various time moments up to $100\,\mu$s for pressure levels of $6.66-10.0$ kPa.

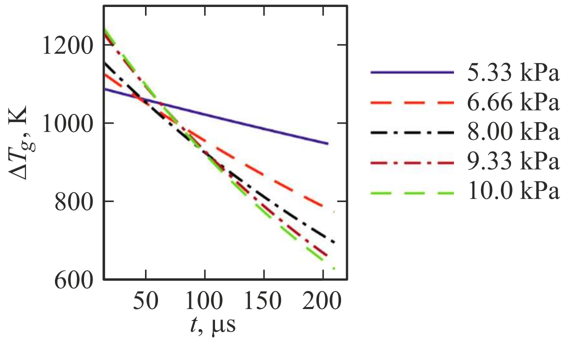

Figure 9. Approximations of the dependences of the overheating temperature of the initiated MW-discharge trace on time for pressures from 5.33 to 10.0kPa.

does not change noticeably for $22\,\mu$s after switching off the microwave radiation.

Experimental data on the overheating temperature of MW-discharge trace (two fringes) from 15 to $100\,\mu$s are shown in Fig. 8 together with data from the numerical analysis (maximum in the calculated range). The interferometer readings, taking into account uncertainty and calculations, are consistent at least for the first $20-25\,\mu$s: the calculated curve hits the red dots. Further, the model shows a faster decrease in temperature, which is more noticeable with increasing pressure. The discrepancy may be due to ignoring the rapid heating mechanism, which creates a time-consuming (tens of μs) heating due to the accumulated excited states of components in plasma exceeding the equilibrium amount. Based on the above, it can be concluded that the model is suitable for describing the temperature of a trace at low pressures and at short times after disconnection.

It is useful to obtain an analytical dependence of the trace overheating temperature on time and pressure at the selected parameters of the laser and microwave system. Approximations of temperature versus time at different pressures are built based on the first line data of the interferometer (Fig. 9). Damped exponential curves are chosen as the approximation function.

$$\Delta T_g = A\exp(-Bt).$$

The typical temperature drop time lies in the range of $300-1000\,\mu$s. At higher pressure, the trace cools faster. Further it was found that approximation coefficients $(A,\,B)$ depend on pressure in approximately linear way. This is how a general approximation of temperature versus time with pressure-dependent parameters was obtained.

$$\Delta T_g(p_g,t) = \left(45.9\left[\frac{\mathrm{K}}{\mathrm{kPa}}\right]p_g + 851.5[\mathrm{K}]\right) \times \exp\left(-\left(\frac{526p_g}{1[\mathrm{kPa}]} - 1800\right)\frac{t}{1[\mathrm{s}]}\right).$$

Conclusion

As part of the study, information was obtained on the temperature dynamics of a microwave discharge trace with a sparkless laser initiation. The trace corresponds to a filamentous microwave discharge, which is rapidly produced in units of microseconds at low pressure precisely due to laser initiation.

As the pressure increases, the laser radiation is absorbed more strongly, which leads to formation of a longer discharge filament in the microwave field. At pressure of 5.33 kPa the microwave energy of 18.2 mJ is put into the entire plasma, and 1.4 mJ into the ionized air (by the end of the MW-pulse), which resulted in heating of the discharge trace to 5000 K in an area 4 mm long, 1 mm in diameter. An increase in pressure led to a narrowing and elongation of the discharge trace to 8 mm, it turned out to be hotter (6000 K), despite a decrease in total energy input to 6.7 mJ, of which 0.4 mJ — directly into the medium by the end of the microwave pulse.

The trace temperature decreases twofold during the first $3\,\mu$s after the MW-radiation is turned off. After that, the temperature varies more slowly. The trace with a temperature of about 1100–1300 K exists during $1000\,\mu$ s at pressure level of 5.33 kPa, $300\,\mu$s at pressure level of 10.0 kPa. The empirical dependence of the trace temperature on time and pressure of the medium is derived.

The temperature of the trace is compared by simulation and from experiment. The numerical model used is a development of the well-known microwave plasma models; laser initiation has additionally been taken into account. Calculations of the trace decay qualitatively and quantitatively at short times of about $10-20\,\mu$s are consistent with the interferometer readings. We believe that this model, in general, may pass the validation. It can be refined by adding a rapid heating mechanism to describe the dynamics of the trace at later stages of the decay.

Funding

Numerical modelling of gas dynamics is consistent with MW-plasma dynamics under laser radiation and the experimental studies were supported by grant from the Russian Science Foundation № 23-19-00241.

Conflict of interest

The authors declare that they have no conflict of interest.

References

[1] D.L. Kuznetsov, V.V. Uvarin, I.E. Filatov. J. Phys. D: Appl. Phys., **54** (43), 435203 (2021). DOI: 10.1088/1361-6463/ac17b2

[2] L. He, U. Zhang, H. Zeng, B. Zhao. Chinese J. Aeronautics, **36** (12), 53 (2023). DOI: 10.1016/j.cja.2023.04.029

[3] S. Starikovskaia, D.A. Lacoste, G. Colonna. Europ. Phys. J. D, **75** (8), 231 (2021). DOI: 10.1140/epjd/s10053-021-00240-2

[4] A.Y. Starikovskiy, N.L. Aleksandrov. Plasma Phys. Reports, **47** (2), 148 (2021). DOI: 10.1134/S1063780X21020069

[5] O.A. Azarova, O.V. Kravchenko. Energies, **17** (7), 1632 (2024). DOI: 10.3390/en17071632

[6] Yu.P. Rajzer. *Fizika gazovogo razryada* (Intellekt, Dolgoprudny, 2009), p. 736. (in Russian).

[7] J.P. Boeuf, B. Chaudhury, G.Q. Zhu. Phys. Rev. Lett., **104** (1), 015002 (2010) DOI: 10.1103/PhysRevLett.104.015002

[8] A. I. Sayfutdinov Candidate's Dissertation in Mathematics and Physics (Kazan, Kazan Aviation Institute (2023).

[9] V. Gildenburg, A. Kim. Fizika Plazmy, **6** (4), 904 (1980) (in Russian).

[10] A.L. Vikharev, A.M. Gorbachev, A.V. Kim, A.L. Kolysko. Plasma Physi. Fusion Technol., **18** (8), 554 (1992).

[11] V.A. Bityurin, V.G. Brovkin, P.V. Vedenin. Tech. Phys. Lett., **41** (3), 217 (2015). DOI: 10.1134/S1063785015030037

[12] V. A. Bityurin, V. G. Brovkin, P. V. Vedenin. Tech. Phys., **60** (2), 222 (2015). DOI: 10.1134/S1063784215020036

[13] V.G. Brovkin, P.V. Vedenin. J. Appl. Phys, **128** (11), 113301 (2020). DOI: 10.1063/5.0016249

[14] A.I. Sayfutdinov, E.V. Kustova, A.G. Karpenko, V.A. Lashkov. Fizika Plazmy, **45** (6), 568 (2019) (in Russian). DOI: 10.1134/S036729211905010X

[15] Q. Shen, R. Huang, Z. Xu, H. Wei. Appl. Sci., **10** (15), 5393 (2020). DOI: 10.3390/app10155393

[16] Y. Yang, W. Hua, S.Y. Guo. Phys. Plasmas, **21** (4), 040702 (2014). DOI: 10.1063/1.4872000

[17] N.A. Popov. Plasma Sources Sci. Technol., **25** (4), 044003 (2016). DOI: 10.1088/0963-0252/25/4/044003

[18] N.A. Popov, S.M. Starikovskaia. Progr. Energy and Combustion Sci., **91**, 100928 (2022). DOI: 10.1016/j.pecs.2021.100928

[19] Y. Zhu, S. Starikovskaia. Plasma Sources Sci. Technol., **27** (12), 124007 (2018). DOI: 10.1088/1361-6595/aaf40d

[20] A.I. Bechina, E.V. Kustova. Vestnik St.Petersb. Univ. Math., **52** (1), 81 (2019). DOI: 10.3103/S1063454119010035

[21] A.I. Saifutdinov, E.V. Kustova. J. Appl. Phys., **129** (2), 023301 (2021). DOI: 10.1063/5.0031020

[22] N.A. Popov. J. Phys. D: Appl. Phys., **44** (28), 285201 (2011). DOI: 10.1088/0022-3727/44/28/285201

[23] V.S. Popov. UFN, **174** (9), 921 (2004) (in Russian). DOI: 10.3367/UFNr.0174.200409a.0921

[24] V.Yu. Fedorov, V.P. Candidov. Opt. i spektr., **105** (2), 306 (2008) (in Russian).

[25] Y. Kolesnichenko, V. Brovkin, D. Khmara, I. Mashek, V. Lashkov, M. Rivkin. 44th *AIAA Aerospace Sciences Meeting and Exhibit. Reno, Nevada: American Institute of Aeronautics and Astronautics* (2006), DOI: 10.2514/6.2006-792

[26] R.S. Khoronzhuk, A.G. Karpenko, V.A. Lashkov, D.P. Potapenko, I.Ch. Mashek. J. Plasma Phys., **81** (3), 905810307 (2015). DOI: 10.1017/S0022377814001299

[27] J.B. Michael, A. Dogariu, M.N. Shneider, R.B. Miles. J. Appl. Phys., **108** (9), 093308 (2010). DOI: 10.1063/1.3506401

[28] S.D. McGuire, M.N. Shneider. Plasma Phys., (2024). DOI: 10.48550/arXiv.2411.18963

[29] Yu.V. Dobrov, V.A. Lashkov, I.Ch. Mashek, A.M. Prokshin, M.E. Renev, R.S. Khoronzhuk. J. Eng. Phys. Thermophy., **97** (4), 1068 (2024).

[30] C.J. Peters, M.N. Shneider, R.B. Miles. J. Appl. Phys., **125** (24), 243301 (2019). DOI: 10.1063/1.5098306

[31] M.J. DeWitt, R.J. Levis. J. Chem. Phys., **108** (18), 7739 (1998). DOI: 10.1063/1.476208

[32] A. Talebpour, J. Yang, S.L. Chin. Opt. Commun., **163** (1−3), 29 (1999). DOI: 10.1016/S0030-4018(99)00113-3

[33] J. Kasparian, R. Sauerbrey, S.L. Chin. Appl. Phys. B, **71** (6), 877 (2000). DOI: 10.1007/s003400000463

[34] L.C. Lee, G.P. Smith. J. Chem. Phys., **70** (4), 1727 (1979). DOI: 10.1063/1.437690

[35] Biagi database, www.lxcat.net, retrieved on October 28, 2021.

[36] IST-Lisbon database, www.lxcat.net, retrieved on October 28, 2021.

[37] Itikawa database, www.lxcat.net, retrieved on October 28, 2021.

[38] TRINITI database, www.lxcat.net, retrieved on October 12, 2021.

[39] Morgan database, www.lxcat.net, retrieved on October 28, 2021.

[40] BSR database, www.lxcat.net, retrieved on September 29, 2022.

[41] C. Lazarou, A.S. Chiper, C. Anastassiou, I. Topala, I. Mihaila, V. Pohoata, G.E. Georghiou. J. Phys. D: Appl. Phys., **52** (19), 195203 (2019). DOI: 10.1088/1361-6463/ab06cd

[42] F.J. Mehr, M.A. Biondi. Phys. Rev., **181** (1), 264 (1969). DOI: 10.1103/PhysRev.181.264

[43] C. Park, J.T. Howe, R.L. Jaffe, G. Candler. J. Thermophys. Heat Transfer, **8** (1), 9 (1994). DOI: 10.2514/3.496

[44] NIST Chemistry WebBook [Electronic resource] URL: https://webbook.nist.gov/chemistry/

[45] O. Schenk, K. Grẗner. Future Generation Computer Systems, **20** (3), 475 (2004). DOI: 10.1016/j.future.2003.07.011

[46] G.I. Aseev. *Ispol'zovanie interferometra Makha-Tsendera dlya opredeleniya prostranstvennogo raspredeleniya pokazatelya prelomleniya i temperatury v plameni* training guide (Phys.fac.) SarGU, Saratov, 2005) p. 30 (in Russian).

Translated by T.Zorina